Bull. Spec. Astrophys. Obs., 2002, 54, 74–88

Reduction of CCD observations with scanning Fabry-Perot interferometer

A.V. Moiseev

Special Astrophysical Observatory of the Russian AS, Nizhnij Arkhyz 369167, Russia

Received March 18, 2002; accepted July 11, 2002.

Abstract. The algorithms used for reduction of data obtained in a Fabry-Perot interferometer mode of the new focal reducer of the 6 m telescope SCORPIO are described. The main attention is focused on the procedures of photometry correction of channels and night sky emission subtraction, which is especially important for observations with a CCD in comparison with a photon counter. The influence of various sources of errors on measurements of radial velocities in a data cube is investigated. Examples of velocity field construction by using emission lines in the galaxy NGC 6951 and absorption lines in the globular cluster M 71 are presented.

Key words: Instrumentation: interferometers — scanning Fabry-Perot: data reduction

1. Introduction

The scanning Fabry-Perot interferometer (IFP) is a highly efficient device for investigation of kinematics of extended objects by the method of two-dimensional spectroscopy. Observations with the IFP consist of successive acquisition of a few dozen images of interference rings from the object (or from a calibration lamp) when changing the optical path between the plane-parallel plates. The radius of the rings is a function of wavelength and gap between the plates of the interferometer. The complete set of such images which fills the free spectral range of the interferometer is called a scanning cycle. After a special reduction, these images may be represented as a data cube. In this cube, X and Y ("spatial coordinates") correspond to the coordinates in the picture plane, while the wavelengths (or Doppler velocities in a fixed spectral line) are a third "spectral coordinate" Z (see Fig. 1). For observations of galaxies, such a technique was first applied by Tully (1974) in studying the motions of ionized gas in M51 in the H_α line. A photographic plate was used as the detector. In the following two decades the systems with the scanning IFP were employed in observations at many big telescopes (TAURUS-2 at the 4.2 m telescope WHT (Spain), PUMA at the 2.1 m telescope of OAN (Mexico), CIGALE at the 3.6 m telescope (ESO), the project KTS for the Japanese 8.2 m telescope SUBARY, etc.). The study of two-dimensional kinematics of galaxies at the 6 m telescope of SAO RAS with the use of the scanning IFP was started by a group of researchers from Marseille Observatoire in cooperation with the colleagues from SAO in the first half of 1980s (Boulesteix et al., 1982; Amram et al., 1992; Dodonov et al., 1995). The observations were made with the system CIGAL which consisted of a focal reducer with the IFP and a two-dimensional photon counter IPCS as the detector. The IPCS was replaced by a low readout noise CCD in 1997, and in the fall of 2000 the first observations with a new multimode optical reducer SCORPIO (Spectral Camera with Optical Reducer for Photometrical and Interferometrical Observations) were carried out. As compared with the old reducer, the SCORPIO is fully automated, its transmission is several times as high, and the optics for accurate calibration is better.

In the present paper we describe the procedure adopted for the reduction of observations with the SCORPIO in the IFP mode. At the present time, there are available several extensively used programmes of reduction of this kind of data. First of all, this is the package ADHOS developed by Boulesteix (2000) and the package of programmes operated under the IRAF (see Gordon et al., 2000). However, in our opinion, in the programmes mentioned the specific character of observations with a CCD, in which the contribution of the atmosphere in the data cube varies from frame to frame, is not adequately taken into account. This leads to the appearance of systematic errors and artifacts in the construction of radial velocity fields. Note that this problem is obviated in observations with the photon counter which makes short exposures and thereby eliminates the effect of the atmosphere. The new procedure of reduction of CCD images that we developed takes account of the effect of the atmosphere and improves the radial ve-

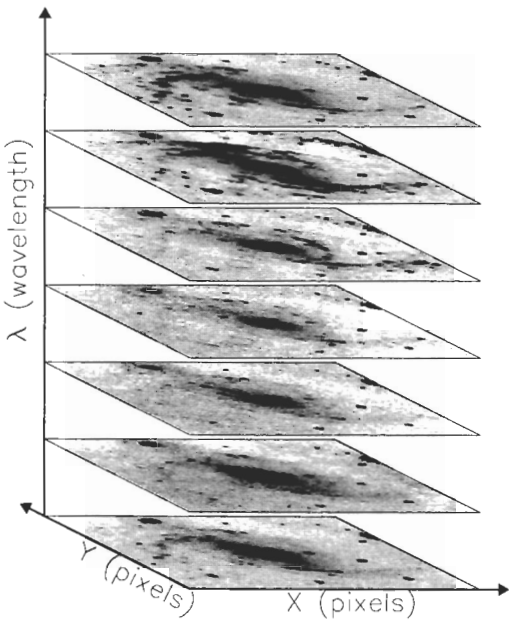

Figure 1: *An example of the "data cube" obtained with the IFP. Every fourth channel along the wavelength λ is shown.*

locity measurement accuracy.

The basic data from the theory of the interferometer are presented in Section 2.1. The present-day facilities used for IFP observations of SAO and the problems arising with the application of CCDs are discussed in Sections 2.2 and 2.3. The primary reduction of observations and the conversion of the data cube to the wavelength scale are described in Sections 3 and 4. The sources of errors affecting the radial velocity measurement accuracy are explored in Section 5. The final Section (6) gives results of observations of two objects.

2. Fabry-Perot interferometer of SAO RAS

2.1. Principal relations

The theory of the Fabry-Perot interferometer as applied to astronomical investigations is stated in detail in a number of papers (Courtes, 1960; Bland and Tully, 1989; Gordon et al., 2000). Below we will present a few necessary relations. If a parallel monochromatic beam of light with a wavelength λ strikes the interferometer at an angle ϑ with respect to the optical axis, the condition of maximum of the interference pattern is then written as

$$n\lambda = 2l\mu\cos\vartheta = \frac{2l\mu}{\sqrt{1+\left(\frac{r}{f}\right)^2}}. \qquad (1)$$

Here n is the order of interference, l is the distance between the interferometer plates, μ is the refractive index of the medium between the plates. The optical system (a camera with a focal length f) constructs the image of the interference rings on a two-dimensional detector (Fig. 2). Differentiating (1), we obtain an expression for the angular dispersion:

$$\frac{d\lambda}{d\vartheta} = -\frac{2l\mu}{n}\sin\vartheta = -\frac{2l\mu}{n}\frac{1}{\sqrt{1+\left(\frac{f}{r}\right)^2}}. \qquad (2)$$

It follows from (2) that, firstly, the dispersion grows towards the centre of the rings, and, secondly, the width of the rings decreases with increasing radius r. The distance between the adjacent orders of interference defines the free spectral range of the IFP:

$$\Delta\lambda = \lambda/n. \qquad (3)$$

An important characteristic property of the IFP is its finesse:

$$F = \Delta\lambda/\delta\lambda, \qquad (4)$$

where $\delta\lambda$ is the halfwidth of its instrumental profile which defines the spectral resolution and depends, first of all, on the characteristics of the reflective coatings of the IFP.

For the scanning interferometer $2\mu l = A + Bz$, where z is the number of the spectral channel, A and B are certain constants (Gordon et al., 2000). One can easily find that

$$B = \frac{A}{n n_z}, \qquad (5)$$

where n_z is the number of channels in the scanning cycle.

Only the regions for which condition (1) is satisfied will be seen in the image of an extended object in channel z. Thus, spatial and spectral information is mixed in each frame, so that a certain wavelength λ corresponds to the point (x,y). From (1), taking into account that $r \ll f$ and according to (5) $A \gg B$, we obtain an expression for the number of the channel in which the interference maximum is observed at the given radius:

$$z(r) \cong \frac{n}{B}\lambda + \frac{A}{2Bf^2}r^2 - \frac{A}{B}. \qquad (6)$$

The distribution of the quantity $z(x,y)$ in the image plane for the calibration lamp line is generally called the *phase shift map*, and the procedure of transition from z to λ is the *phase correction*. An example of such a map is displayed in Fig. 3. Expression (6) shows that the phase shift in a first approximation is proportional to the square of the distance from the centre of the rings.

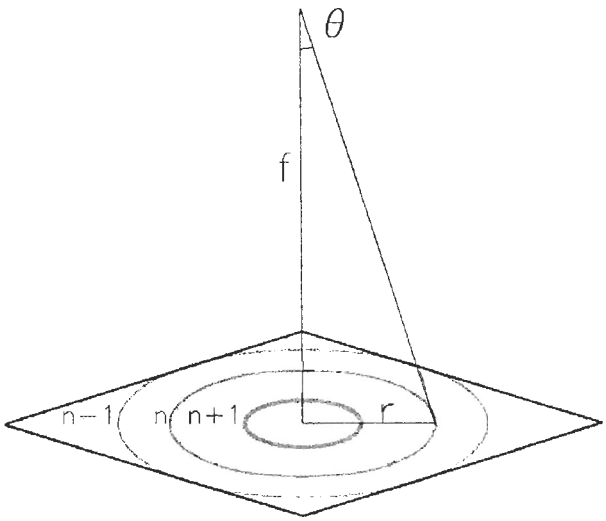

Figure 2: *Interference pattern from monochromatic light. Different rings correspond to different interference orders (n-1, n, n+1).*

2.2. IFP mode with the SCORPIO

The new multimode optical reducer SCORPIO was made at SAO in 2000 (Afanasiev et al., 2002). We will briefly describe here the potentialities of the SCORPIO in interferometric observations. The basic optical components of the SCORPIO are: a collimator $F/2.2$ and a camera $P/1.8$, the total optical efficiency of the system at the prime focus of the 6 m telescope is $F/2.9$. The optics of the reducer compensates for the aberrations of the main mirror of the telescope, all optical surfaces are made untireflecting in a range of $0.35-1.0\mu$. There are two filter wheels, one is in the focal plane of the telescope, the other is between the field lens and collimator. When observing with the IFP, the desired spectral range is cut out with the aid of interference filters with a $FWHM \approx 10 \div 15$ Å placed in the filter wheel near the focal plane. Presently, a set of filters with a maximum transmission of 60 – 80% is used, which are centered on the H_α line in galaxies with systemic velocities from -200 to $+10000\,\mathrm{km \cdot s^{-1}}$. A similar set is manufactured for observations in the line [OIII]λ5007.

A piezoelectric IFP ET-50 produced by the company Queensgate is installed between the collimator and camera, where the exit pupil of the optical system is located. The parameters of the imployed interferometers are presented in Table 1. In 2000–2001 a CCD system Tecktronix 1K × 1K with a readout noise of $3\bar{e}$ was used in observations. This detector provided a field of view of about 5′ at a scale of 0.28″/pixel. A new CCD of 2K×2K is planned to be installed in 2002. The total quantum efficiency of the SCORPIO in observations with the Fabry-Perot (telescope + filter + IFP + CCD) is about 20% in the H_α region.

Table 1: *SCORPIO parameters in IFP mode*

	Queensgate IFP	
	FP260	FP500
range	5000 ÷ 7000 Å	5000 ÷ 8000 Å
n^a	235	501
$\delta\lambda^a$	2.5 Å	0.7 Å
$\Delta\lambda^a$	29 Å	13 Å
F^a	11	17
n_z	24 ÷ 32	32 ÷ 40

[a] values are given for the wavelength 6563 Å

The optical reducer is mounted on the general-purpose platform of the prime focus, which contains two movable bundles of fibers for the off-axis guiding, lamps for the calibration of the wavelength scale (a He-Ne-Ar lamp) and for flat-fielding (a continuous spectrum lamp). The lamps are placed in an integrating sphere providing uniform illumination of the field. The calibration beam forms at the input of the reducer a beam of an aperture ratio of $F/4$, equivalent to that of the telescope. Such a scheme of illumination with equal filling of the output pupil in observations and calibration ensures the absence of shift when measuring radial velocities. This was confirmed by real observations with the IFP on the 6 m telescope (see Sections 5.1 and 6.2).

2.3. Comparison of the photon counter and CCD

In observations with the photon counter one executes several dozen cycles of scanning with a very short exposure (10–20 s) in each channel of the IFP. In this fashion one can manage to average the influence of the atmospheric extinction at different zenith distances and the instabilities of seeing with long total exposures. The CCD chip has a considerably higher quantum efficiency as compared to the photon counter. However, the presence of the readout noise does not permit very short acquisition time, and the readout time diminishes the useful exposure time. The use of low-noise CCDs makes it possible to slightly improve the situation. Employing relationship (3) from the paper by Bland and Tully (1989), we compared the capabilities of the SCORPIO in reaching a maximum possible S/N ratio, when using our "thin" CCD TK 1024 (the readout noise is $3\bar{e}$, the maximum quantum efficiency is ∼ 80% at λ6500 Å) and using a present-day photon counter with a GaAs cathode and maximum quantum efficiency ∼ 25% (Hernandez et al., 2001). The calculations were performed for the observations at the prime focus of the 6 m telescope with the system SCORPIO. In a wide range of intensities of objects, the CCD reaches a larger S/N ratio only if the acquisition time exceeds the readout time

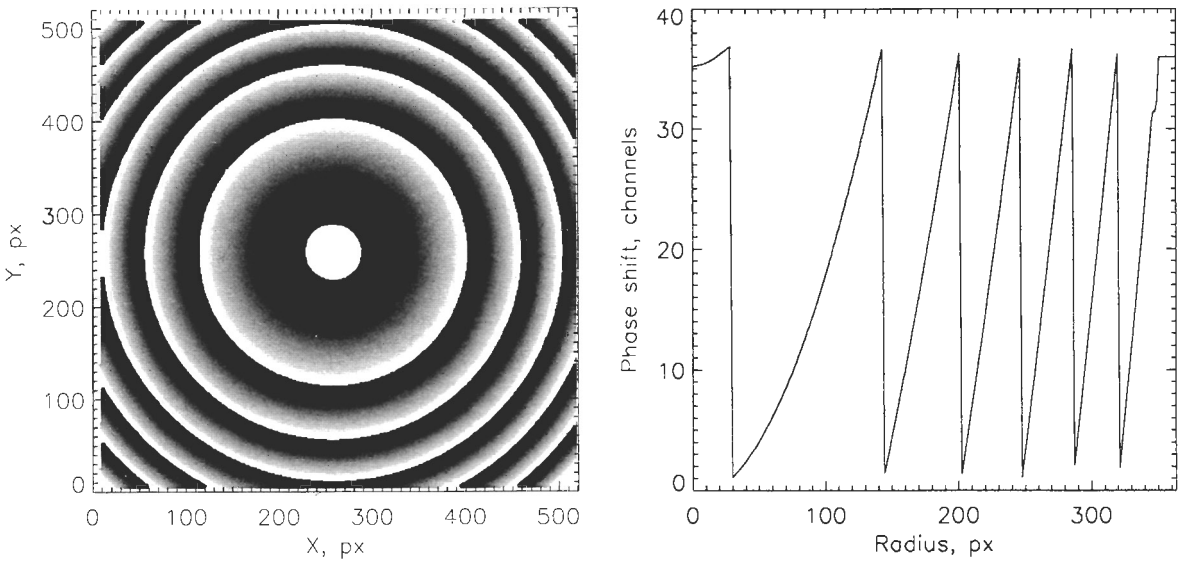

Figure 3: *Map of phase shifts for FP501 (left panel). Radial variation of the phase shift in units of spectral channel (right panel).*

($T_{exp} > T_{readout}$). However, if $T_{exp} \simeq T_{readout}$, the observing time is then spent inefficiently because half of it will be spent for readout of the signal from the CCD. Now $T_{readout}$ is equal to 20 s in the mode with binning 2 × 2, and to 90 s with binning 1 × 1. This is why, with the CCD one has to make exposures of several minutes in each channel of the IFP. But here a problem arises of taking into account the variations of atmospheric transparency and seeing in individual CCD frames (photometric correction), because in reality only 1–2 scanning cycles can be performed. Because of this, with the advent of highly sensitive photon counters superior to CCD at short exposures, they start to be extensively used for observations with the scanning IFP (Hernandez et al., 2001). At the same time, the modification of the method of photometric corrections of CCD frames (Section 3.4) allows one to make use of the advantages of CCDs at long exposures.

3. Preliminary reduction and photometric correction

3.1. Raw data

The following sets of CCD frames are original for reduction (see the block diagram in Fig. 4).

• **OBJECT** — interferograms of the object under investigation. It is recommended to observe first the images in the odd channels of the interferometer (1, 3, 5...), then in all even ones (2, 4, 6...). This is done in order to avoid systematic errors in evaluating the variations of atmospheric transparency and seeing.

• **NEON** — images of interference rings from the emission line cut out by a narrow-band filter from the spectrum of the built-in He-Ne-Ar lamp. The calibration is generally performed before and after the observing night.

• **FLAT** — interferograms of uniform illumination of the "flat field" from the built-in continuous spectrum lamp, obtained with the same narrow-band filter as was used in observing the object.

• **TEST** — images of the rings from the He-Ne-Ar lamp in individual channels of the IFP which are obtained every 30–60 minutes during the exposure of the object. They are used for monitoring the scanning accuracy of the interferometer (the characteristics of which, generally speaking, depend on time) and for checking the shifts of the centres of the rings of the interference pattern, which arise because of flexures of the apparatus. In the case of SCORPIO the shift of the centre of the rings caused by flexures of the system reducer–CCD does not exceed 0.5 pixel in the whole range of variations of zenith distances.

Bias frames (**BIAS**) and dark frames (**DARK**) "standard" for CCD observations are also needed.[1]

3.2. Building of data cubes and flat fielding

The **BIAS** frames are averaged as in ordinary CCD reduction. The frame SUPERBIAS obtained as a result of averaging is subtracted from all frames and calibrations. Defective columns in the frames are

[1] We will not speak further about taking account of the dark frames, since in the CCD we use it is about 0.1$\bar{e}$/min, i.e. it is insignificant at short exposures.

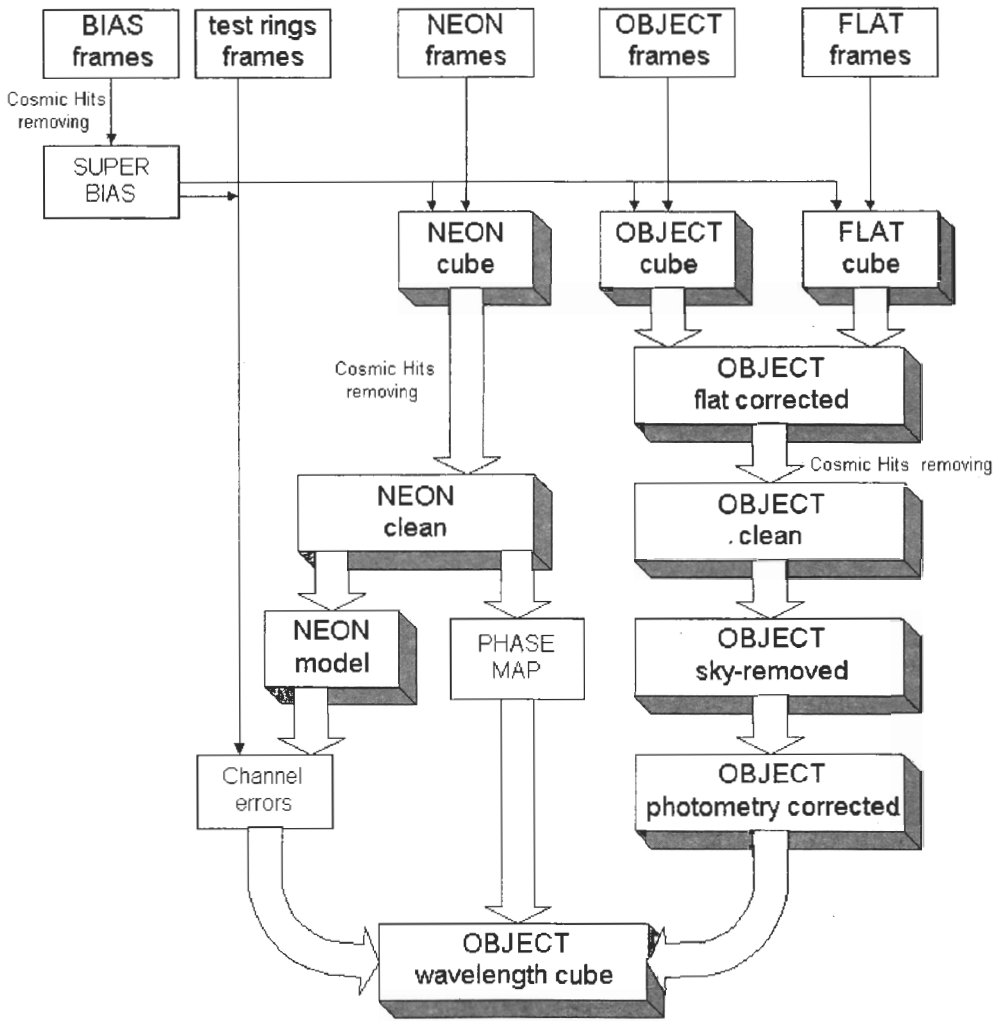

Figure 4: *Block diagram of data reduction*

masked. Further processing is performed not of the two-dimensional frames but of the three-dimensional cubes (a set of object's and calibrations' frames). The removal of cosmic hits in the cubes is done by a simple σ-filter: the counts in individual spectra which differ from the mean by a threshold value (on the scale of standard deviations) are replaced by the half-sum of the neighbouring ones. Preliminarily, the cube **OBJECT** is normalized to the cube **FLAT**, which makes it possible to take into account two effects at once: firstly, the sensitivity variations of the CCD pixels and optics throughput over the field of view (photometric "flat field"), secondly, the spectral modulation introduced by the narrow-band filter, which changes over the detector field since the central wavelength of the interference filter depends on the angle of the beam incidence. Because of this, it is important that the angle of convergence of the beam from the calibration lamp should be close to the angle of convergence of the beam from the telescope. In other words, the filling of the output pupil for the object and calibration must be equal. This condition (the condition of telecentrism) is met in the SCORPIO by using special optics in the calibration beam. The violation of the condition of equivalency of the pupils leads, first of all, to shifting the spectra in wavelength in the cube **FLAT**. A correct reduction of such data (obtained with the old version of the optical reducer) is possible provided that there are bright enough stars in the field, the spectrum of which can be regarded as "flat" in a range of 10–20 Å. In this case the shift in λ is defined from the cross-correlation of spectra of stars and flat field (preliminarily corrected for the phase shift). After that a shift of spectra by the required number of spectral channels was performed in the cube **FLAT**, and the cube derived was used for normalizing **OBJECT**. We will emphasize that in this case the normalization to **FLAT** should be accomplished before the procedures of photometric and phase correction. The residual modulation is corrected after the conversion of the cube to the wavelength scale.

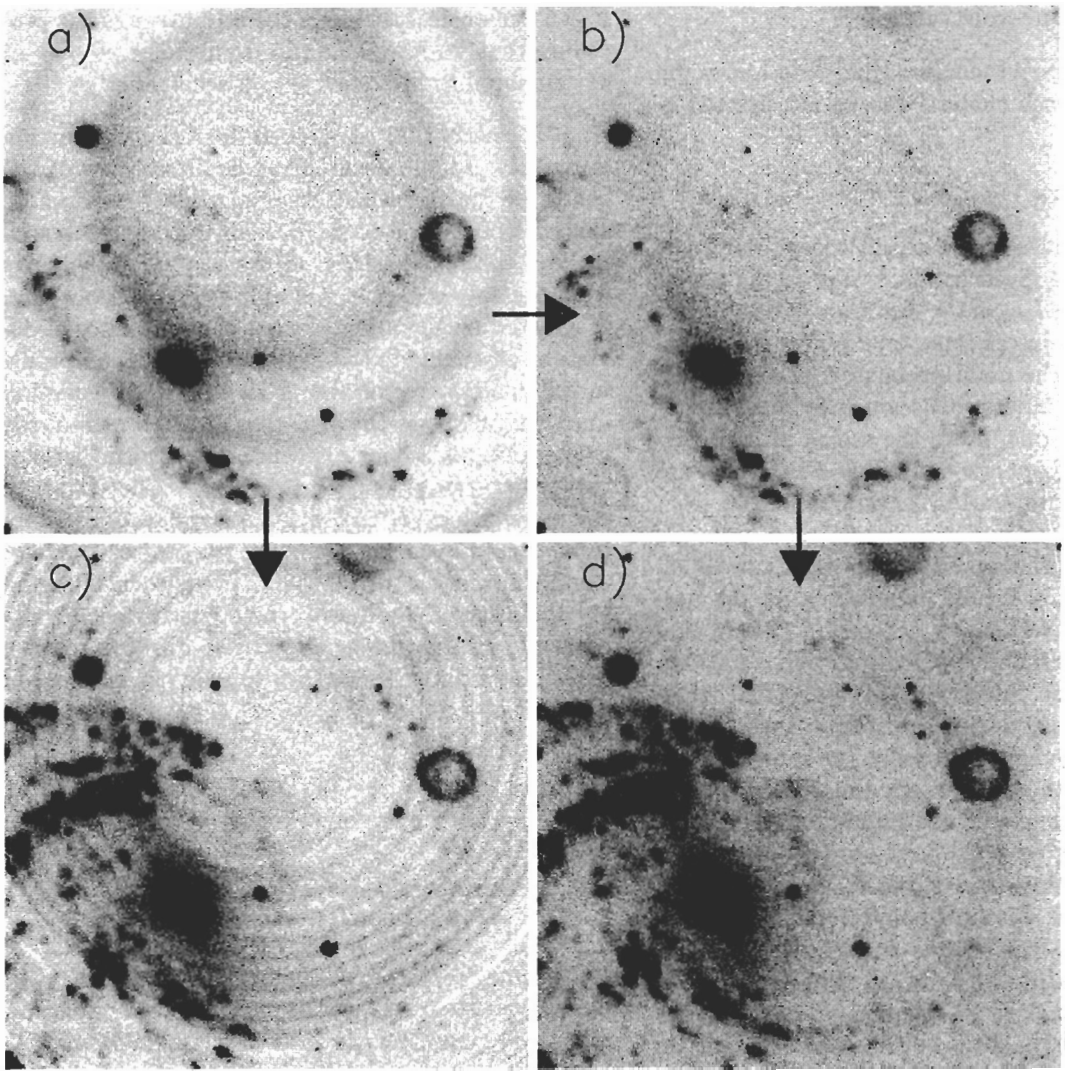

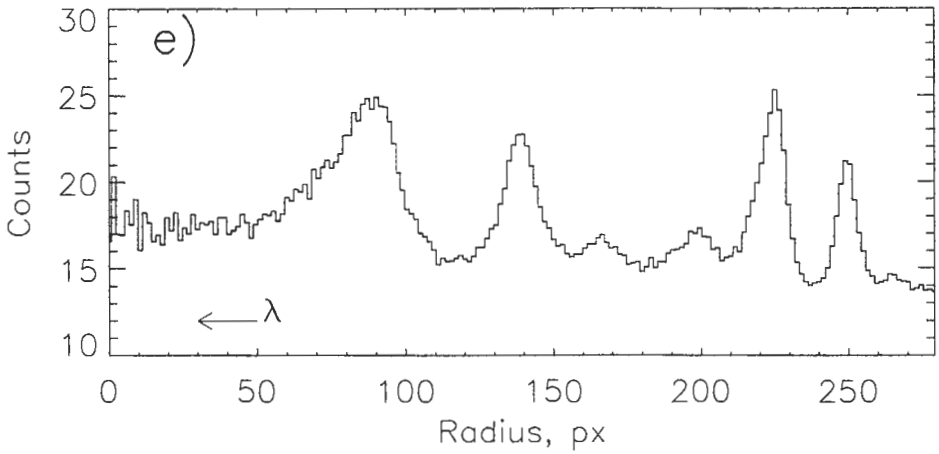

Figure 5: *Observations of the galaxy NGC 6951 in the H_α line with the SCORPIO: a) a fragment of the spectral channel with rings from the sky lines; b) the same frame after sky subtraction; c) the spectral channel on the wavelength scale, which was obtained after the phase correction of the cube with the sky (Method I); d) analogous channel after the phase correction of the cube with the sky subtracted (Method II), the arrows indicate the sequence of reduction in each of the method; e) the radial profile of the night sky spectrum, the arrow indicates the dispersion direction.*

3.3. Night sky line subtraction

After the preliminary reduction described above the observed flux in each channel can be represented in the form

$$I_{obs}(x,y) = (I_{obj}(x,y) \odot PSF) * Ext + I_{sky}(r), \quad (7)$$

here I_{obj} is the image of the object corrected for the atmosphere in the given channel, Ext is the atmospheric extinction, I_{sky} is the flux from the night sky modulated by the interferometer, PSF is the point-spread function. The main problem is presented by: the night sky brightness (emission spectrum, illumination from the Moon, etc.), the seeing provided by PSF and the atmospheric extinction Ext, which are dependent on the time of observations. Apart from the smooth constant variations connected with the zenith distance variations, random variations of all these quantities are also of importance. In the universally accepted scheme of processing (Bland and Tully, 1989; Boulesteix, 2000; Gordon et al., 2000), channel-by-channel correction of the seeing and atmospheric transparency is performed first, then follows the phase correction, while the sky line subtraction is accomplished on the wavelength scale. Further, this method will be designated as Method 1. The scheme is ideal when working with the photon counter, when the atmospheric effect is averaged in each channel by multiple exposures. In observations with CCD, such a technique is applicable when working in a spectral range free from night sky emission lines. However, it is not infrequent that variations of intensities of night sky lines lead to the fact that on the wavelength scale the profile of the sky emission lines varies with radius r. In other words, in the wavelength domain, artifacts — contrast rings — appear in the channels **OBJECT**. This imposes restrictions on the measurement accuracy of velocities from weak emission lines of the object and causes systematic errors in their estimations (Section 5.2).

For this reason, we proposed a method of sky subtraction in each image prior to the phase correction (hereafter Method II). In the detector regions free from the emission of the object the night sky lines are averaged by the azimuthal angle in the narrow rings of 0.5–1 pixel wide with the centre on the optical axis of the IFP (Fig. 5). The derived radial profile (Fig. 5e) is subtracted from the image (Fig. 5a,b). By repetition of this procedure in all the channels one can correctly get rid of the effect of the second term in (7) without introducing distortions in the wavelength domain.[2] Fig. 5 demonstrates clearly the advantage of the procedure that we have adopted (sequence $a \rightarrow b \rightarrow d$) as compared to Method 1 (sequence $a \rightarrow c$).

It is clearly that the procedure of sky subtraction is sensitive to the accuracy of determination of the centre of the rings (see Section 5.2) which may be shifted from frame to frame. For automated search for an optimum position of the centre of the rings from the sky, we apply a simple iterative procedure. It is based on the minimization of the squares of deviations of counts in the pixels from the mean profile in the detector region free from the object emission lines. Fig. 6 shows the variation of the centre of the rings during a 2-hour exposure, the zenith distance being varied from $z = 15°$ to $z = 45°$. The scatter of points with respect to the main trend is most likely to be caused by errors of finding the centre. They are usually not larger than 0.05–0.2 pixels (depending on the intensity of sky lines), which is sufficient for accurate sky subtraction. Fig. 6 also displays relative variations of intensities of sky lines in observations of different objects.

3.4. Photometric correction

Photometry of stars in the field of view makes it possible to evaluate the contribution of atmospheric instability and guiding errors in each channel **OBJECT**. With the aid of approximation by two-dimensional gaussians relative shifts of the image centre, variations of the $FWHM$ and integral flux are determined for each star. The variation of these parameters vrs the channel number in IFP observations with the SCORPIO found from 12 stars are shown in Fig. 7. The frames' off-sets with respect to one another connected with the telescope guiding errors do not exceed $0.2'' - 0.5''$ and are corrected by the corresponding shifts of the frames (see Fig. 7). To correct the seeing, the frames are convolved with two-dimensional gaussians, so that the resulting $FWHM$, the same as in a frame with the worst images could be obtained. $FWHM$ variations of several tens of per cent are thus diminished to 1–5 %, although, on the whole, the spatial resolution in the cube becomes worse (Fig. 7). Variations of atmospheric transparency are allowed for under the assumption that the continuum in stars is flat in the narrow spectral range being explored. In general, this is not always the case (especially around the H_α absorption). However, if 8–10 stars located at different r are used, the mean flux variations correspond, as a rule, to the extinction variations and do not depend on spectral features in stars.

[2] When this paper was submitted to the press, a paper of Jones et al. (2002) came out, in which the authors used an analogous procedure for sky subtraction in working with adjustable filters, which is a variety of the IFP operated in small orders of interference.

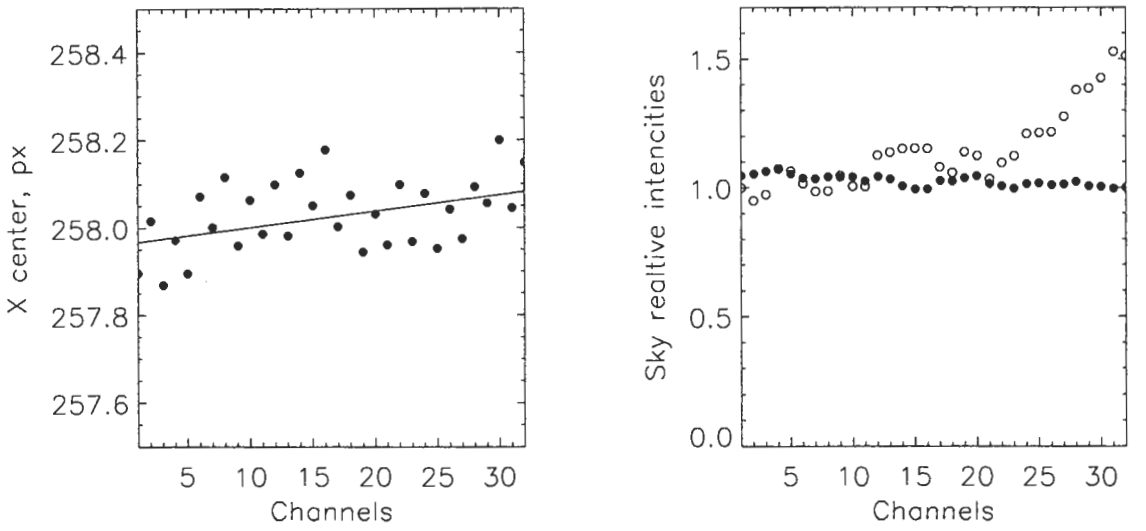

Figure 6: *Measurements of the position of the centre of the rings from the sky in the object cube (left panel). Measurements of the relative night sky line intensities in observations on different nights (black dots and circles).*

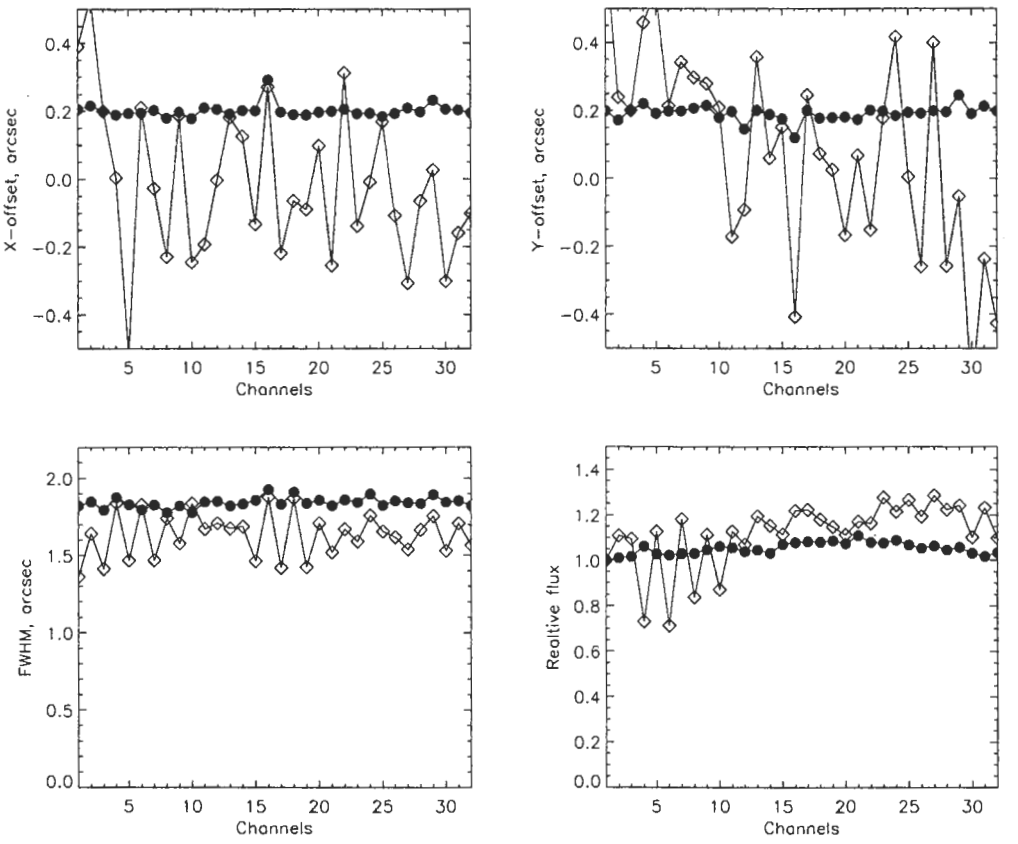

Figure 7: *Variations of the mean parameters of the field stars: relative shifts of barycentres along X and Y, the seeing, integral flux in relative units. The open and filled symbols correspond to the observations of NGC 6951 before and after the photometric correction.*

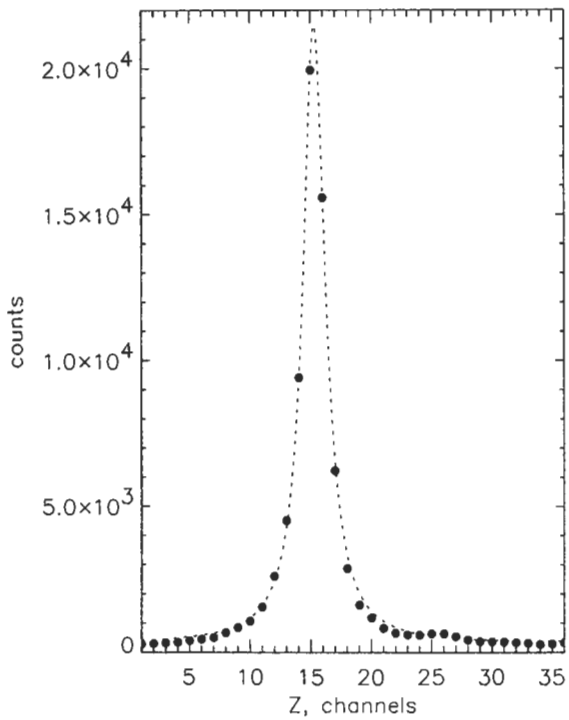

Figure 8: *An example of the spectrum of the calibration line HeIλ6678 scanned with the interferometer Fp500 (dots) and its fitting by the Lorentz profile.*

4. Wavelength scale calibration

4.1. Phase map

According to (6), all the spectra in the observed cube are shifted linearly (to an accuracy of a factor of $(r/f)^4$) by the value of the phase shift with respect to a certain initial wavelength. For determination of the phase shift the Lorentz profile was inscribed into the calibration line spectrum in each point (x, y) of the cube **NEON**:

$$I(x,y,z) = \frac{I_o(x,y)}{1 + \left(\frac{2(z-p(x,y))}{w(x,y)}\right)^2}, \qquad (8)$$

which, according to Bland-Hawthorn (1995), is a much better approximation of the instrumental profile of the IFP as compared to the gaussian one. Here $w(x, y)$ is the line width, while $p(x, y)$ is the phase shift sought for. An example of the distribution p over the field is displayed in Fig. 3.

4.2. Channel-by-channel correction

The method described above is used to find the phase shift assuming that the quantities A and B that relates the channel number z to the gap between the plates (see Section 2.1) are constant in the course of scanning. There are, however, a number of factors, such as temperature variations, errors and failures in the electronics of control, which have an effect on the scanning stability. For control of mutual shifts of the calibration channels for each frame of the cube **NEON**, the best position, with allowance made for the shifts in all three coordinates inside the model cube $I(x, y, z)$ constructed in acordance with (8), is sought by the least squares method. For the IFP operating steadily the scatter of scanning errors in z inside one cube does not exceed 1–3 % and does not affect the quality of data. Over the past 2 years of observations, channels with scanning errors of 10–20 %, which are probably caused by noises in the electronics, were present only two times in the calibration cube. The above-described procedure revealed and removed systematic differences of $\simeq$ 10 % between the scanning step and the correct value, which were caused by inaccurate selection of the constants A and B in the observations of 2000.

A search for relative shifts of the test images of the calibratin rings **TEST** is fulfilled analogously. Fig. 9 shows the changes of the position of the calibration ring centre during 2 hours of observations. The shift of the centre of the rings is insignificant; one can see a smooth variation of the scanning step by more than 15 % with respect to the calibration cube. This is why, prior to the correction of the phase shift, an appropriate correction in the z coordinate is introduced into the object cube.

5. Estimates of the accuracy of velocity measurements

Here, for the sake of convenience in representation, some estimates will be made in units of the spectral channel, which is $15 - 18\,\mathrm{km \cdot s^{-1}}$ for observations in the H_α line with the interferometer FP501 and $35 - 40\,\mathrm{km \cdot s^{-1}}$ for the interferometer FP235. The error of measurement from the emission line in the cube of the object may be represented as

$$\sigma_{Vel} = \sqrt{\sigma^2_{gaus} + \sigma^2_{\lambda} + \sigma^2_{reduct}}, \qquad (9)$$

where σ_{gaus} is the error of determination of the line centre by the gauss-approximation method defined by the S/N ratio in the line; σ_λ is the accuracy of reduction to the wavelength scale; σ_{reduct} are the errors appearing at the stage of reduction and related, first of all, with provision for the atmospheric instability.

The contribution of σ_{gaus} is small. We have modeled its relation to the S/N ratio by the Monte-Carlo method. For typical line widths ($FWHM = 4 - 10$ channels) and Poisson noises, it turns out that the error of determination of the line centre is $\sigma_{gaus} < 0.05 - 0.08$ of the channel even at a $S/N > 4 - 5$.

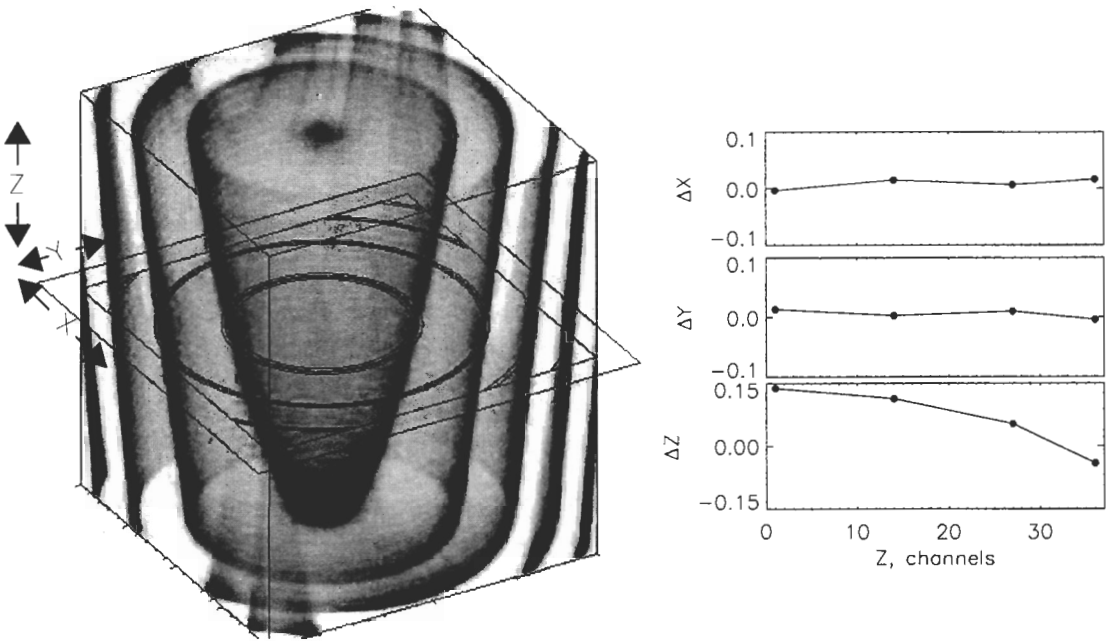

Figure 9: *A schematic view (left panel) illustrating search for the optimum position of the image of the calibration rings inside the model calibration cube. The gradations of the grey show the variations of intensity of the model profile in the cube. Relative shifts of test images (in pixels) relative to the calibration cube during a 2-hour exposure (right-hand panel).*

5.1. Phase correction error

An independent evaluation of the phase shift correction accuracy was performed when measuring velocities of the night sky emission lines in the data cube obtained with the FP501 polarimeter in the observations of M71 (Section 6.2). The lines $H_\alpha\lambda6562.82$ Å and OH$\lambda6568.779$ Å from the adjacent interference order were used.[3] The mean velocity was $2.2\,\mathrm{km\cdot s^{-1}}$ with a point-to-point dispersion of velocities of $2.0\,\mathrm{km\cdot s^{-1}}$, that is, the accuracy of construction of the wavelength scale is about 1.0 channel, or $\simeq 2\,\mathrm{km\cdot s^{-1}}$ for FP501 and $\simeq 4\,\mathrm{km\cdot s^{-1}}$ for FP235.

5.2. Systematic errors

Regions of images from frames with different z are present at each radius r on the image in the spectral channel for the fixed λ. That is why, any frame-to-frame non-uniformity (variations of the sky line intensity, seeing, etc.) leads to the appearance of systematic distortions in the long-wave cube, which is dependent on the radius. In turn, this causes systematic errors (artifacts) in the obtained monochromatic images in the velocity fields too. We present these errors as consisting of several independent components:

$$\sigma^2_{reduct} = \sigma^2_{SKY} + \sigma^2_{SHIFT} + \sigma^2_{FLAT}. \qquad (10)$$

[3] Wavelengths are taken from Osterbrock et al. (1996).

Here σ_{SKY} is the error introduced by the variability of the background and night sky lines, σ_{SHIFT} is the guiding error, and σ_{FLAT} is the error of division by **FLAT**.

The contribution of different components in (10) is estimated with the aid of modeling the process of reduction. Distributions of radial velocity and brightness (disk + nucleus + HII regions) with the parameters typical of the observed galaxies were specified in the sky plane. These data were used to construct the cube in λ domain, and having made a transformation, inverse with (6), we obtained the "observed" cube in z domain. The cube with the rings from the night sky was constructed in a similar manner. By combining the two cubes and introducing in them the required distortions (relative shifts of channels, transmission variation, additional noises, etc.), we constructed the "observed" velocity fields, which were compared with initial velocities. The modeling was performed for the version of observations with FP235. The following results were derived.

• σ_{SKY} was evaluated for different variations of atmospheric extinction and brightness of the night sky lines in the two methods of sky subtraction (Section 3.3) — Method I (in λ domain) and Method II (in z domain). A characteristic relation between the velocity determination error and the line intensity (in units of the brightest sky line A_{sky}) is displayed in Fig. 10. Even at 10–20 % variations of the sky line intensity and extinction, Method II yields a veloc-

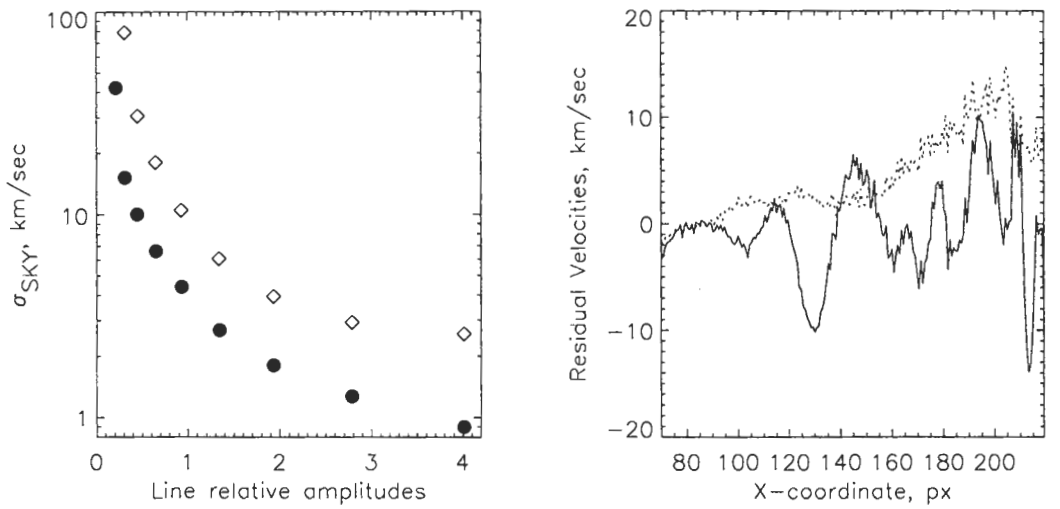

Figure 10: *Modeling of the errors. Left-hand panel — velocity measurement errors as a function of emission line intensities of the object (in units of intensity of the strongest line in the sky) in the case of smooth intensity variations of the sky lines and atmospheric extinction by 20 % during the exposure. The filled and open symbols correspond to sky subtraction before and after the phase correction. Right-hand panel — an example of residual velocities (measurements minus model) along the section across the velocity field. The solid line represents random shifts of the centre of the rings with* $\sigma = 0.5''$*, the dotted line shows the smooth shift of the centre by* $\sigma = 1''$ *during the exposure.*

ity measurement error 2–5 times as low as Method I, which is more essential for weak (with respect to the sky) lines of the object. One may consider that $\sigma_{SKY} < 10\,\mathrm{km \cdot s^{-1}}$ (0.2 channel) even for lines with an amplitude higher than $(0.3 - 0.5)A_{sky}$. The error becomes insignificant (less than $2\,\mathrm{km \cdot s^{-1}}$) for lines with an amplitude $(1.5 - 2)A_{sky}$. Naturally, σ_{SKY} depends on the relative location of the lines of the sky and object in the spectrum, but the accuracies given above may be regarded to be typical. Fig. 10 illustrates the advantage of Method II in the reduction of CCD observations of objects against the background of the bright sky lines. If the intensity of the sky lines is insignificant, the two methods give similar results. When using Method II, it is important to precisely define the position of the centre of the rings. The modeling has shown that σ_{SKY} begins to considerably increase if the error of determining the position of the centre of the rings $\sigma_{CENTER} > 0.3 - 0.5$ pixel (i.e. 0.05–0.08 of minimum halfwidth of the ring from the sky on the image). As was already noted in Section 3.3, this accuracy is provided by the automated procedure of determination of the centre of the rings.

• The errors of guiding and flexure of the instrument lead to mutual shifts between the images in the cube z (see Fig. 7). The correction of this effect from the position of the images of stars in the field causes mutual shift of channels in the wavelength domain. As a result, an error in the determination of velocities σ_{SHIFT} arises. In contrust to σ_{SKY}, it is only slightly dependent on the line intensity and is mainly defined by the distance from the centre of the rings r. Fig. 10 shows velocity variations in the cross-section of the image of the model galaxy for two types of the channel shifts, random from channel to channel (guiding errors) and systematically increasing (result of instrumental flexure). In the first case spurious rings arise, in the second one a constant velocity gradient appears. Table 2 gives the mean amplitudes of spurious velocities depending on the value of shifts of both types. The systematic flexures in the SCORPIO do not exceed $0.2'' - 0.3''$ in the whole range of zenith distances, and the typical guiding errors are of the order of $0.1'' - 0.2''$.

Table 2: *Amplitudes of spurious velocities (in* $km \cdot s^{-1}$*) for different channel shifts*

Shift ($''$)	Type of shift	
	random	systematic
0.05	3.0	2.1
0.10	5.5	2.2
0.25	22	7.0
0.50	25	16
0.75	32	23
1.00	47	30

• The transmission of the interference filter de-

pends on the angle of ray incidence. So, if the light beams from the telescope and the calibration beams do not coincide, the transmission curves of the filter in the cube **FLAT** and **OBJECT** will then be different both in width and in central wavelength. Using the photometry of the stars in the cube **OBJECT**, this effect can be defined and corrected. The division by the non-corrected cube **FLAT** will lead to distortions of the continuous spectrum shape. Possible errors are determined by the relationship between the filter width, 12–18 Å and by the free spectral range $\Delta\lambda$. It can be easily shown that if the spectrum in the cube **FLAT** is shifted by 2–3 channels or its $FWHM$ differs from **OBJECT** by 20 %, perturbations will then arise with a dispersion of 0.15–0.2 and 0.05–0.08 of continuum intensity for FP235 and FP501, respectively (at $\lambda = 6563$ Å with a filter halfwidth of 15 Å). When observing bright emission lines with a weak continuum, this will cause appearance of an insignificant error in measuring the velocity σ_{FLAT}, however, for the objects with a relatively strong continuum, the non-coincidence of the beams from the object and calibration may result in appearance of spurious lines in the spectrum at the background of the bright continuum.

6. Results of data processing

6.1. Emission object

The galaxy NGC 6951 was observed in the course of the first trial of the SCORPIO with the Fabry-Perot interferometer 23/24.IX.2000. The interferometer FP235 was employed. The scanning cycle consisted of 32 frames with an exposure of 120 s for each. To increase the readout rate a binning of 2 × 2 was applied, the resulting pixel size is $\sim 0.56''$. A filter 16 Å wide centered on $\lambda_c = 6596$ Å separated a region around the H_α line of the galaxy. The variations of the seeing and the atmospheric transparency before and after the photometric correction are shown in Fig. 7, those of the sky line intensity are given in Figs. 5 and 6. After the reduction to the wavelength scale, optimum filtration of data was done, i.e. smoothing in the z coordinate by a gaussian with a $FWHM = 1.5$ of the channel and in the (x, y) plane by a two-dimensional gaussian $FWHM = 2 \times 2$ pixels. For this purpose, we used the package ADHOC.[4] After smoothing, the spatial resolution was about $2.7''$.

Apart from the H_α line, the line [NII]λ6582 Å is present in the observed spectrum of the circumnuclear region. Using a fitting by gaussian of the profiles of emission lines, we have constructed the velocity field of ionized gas and a monochromatic image of the galaxy in each line. An example of the velocity field in the H_α line is presented in Fig. 11. In the same figure are shown the examples of decomposition of the profiles of emission lines in the LINER nucleus and the circumnuclear ring of star formation. The velocities that we have measured are fully consistent with the data of Pérez et al. (2000) which they have obtained for this galaxy with three positions of the spectrograph slit.

6.2. Absorption object

The central part of the globular cluster M71 was observed on 12/13.IX.2001 with the device SCORPIO and interferometer FP501 in the line H_α at the request of N.N. Samus and A.S. Rastorguev. The scanning cycle consisted of 36 frames with an exposure of 120 s per frame; the same as in the preceding case a binning of 2 × 2 was applied. The seeing varied from $1.0''$ to $1.7''$ during the observations. In each frame there are present monochromatic images of stars at the wavelengths defined by their coordinates on the CCD according to (1) (if one disregards the phase shift variations on the scale of the image size). After the preliminary reduction and channel-by-channel subtraction of the night sky lines, we made an automatic measurement of fluxes from individual stars. With this end in view, bright isolated stars were used to plot a mean two-dimensional point-spread function (PSF) in each frame. Using the cross-correlation method, the PSF was made coincident with the barycentre of the star, the integral flux was defined by minimization via the least squares method. This simple method proved to be stable enough for tight stellar fields and made it possible to do relative photometry of neighbouring stars with a separation above $2.5'' - 3''$. For measuring velocities we used two different methods. In the first variant, photometry of stars was performed in each channel prior to the correction of the cube for the phase shift. The spectra thus obtained $F_\lambda(z)$ were transformed to the wavelength scale using the phase shift value corresponding to the position of the barycentre of the star on the phase map. In the second variant the channels in the cube of the object were smoothed for reducing to one value of seeing as described in Section 3.4, so that the average size of the images in the cube was $FWHM = 1.75'' \pm 0.03''$. Next, the whole cube was corrected for the phase shift and only then channel-by-channel photometry was done, which resulted in the star spectrum $F_\lambda(\lambda)$. The profile of the absorption line H_α in the spectra was fitted by a gaussian. Thus, velocities of more than 700 stars, down to the 18th stellar magnitude in the V band, were measured in the observed field (see Fig. 12). The two methods of extraction of spectra of stars yielded close results

[4] The package ADHOC was written by Boulesteix (2000) in Marseille Observatoire and is available in INTERNET.

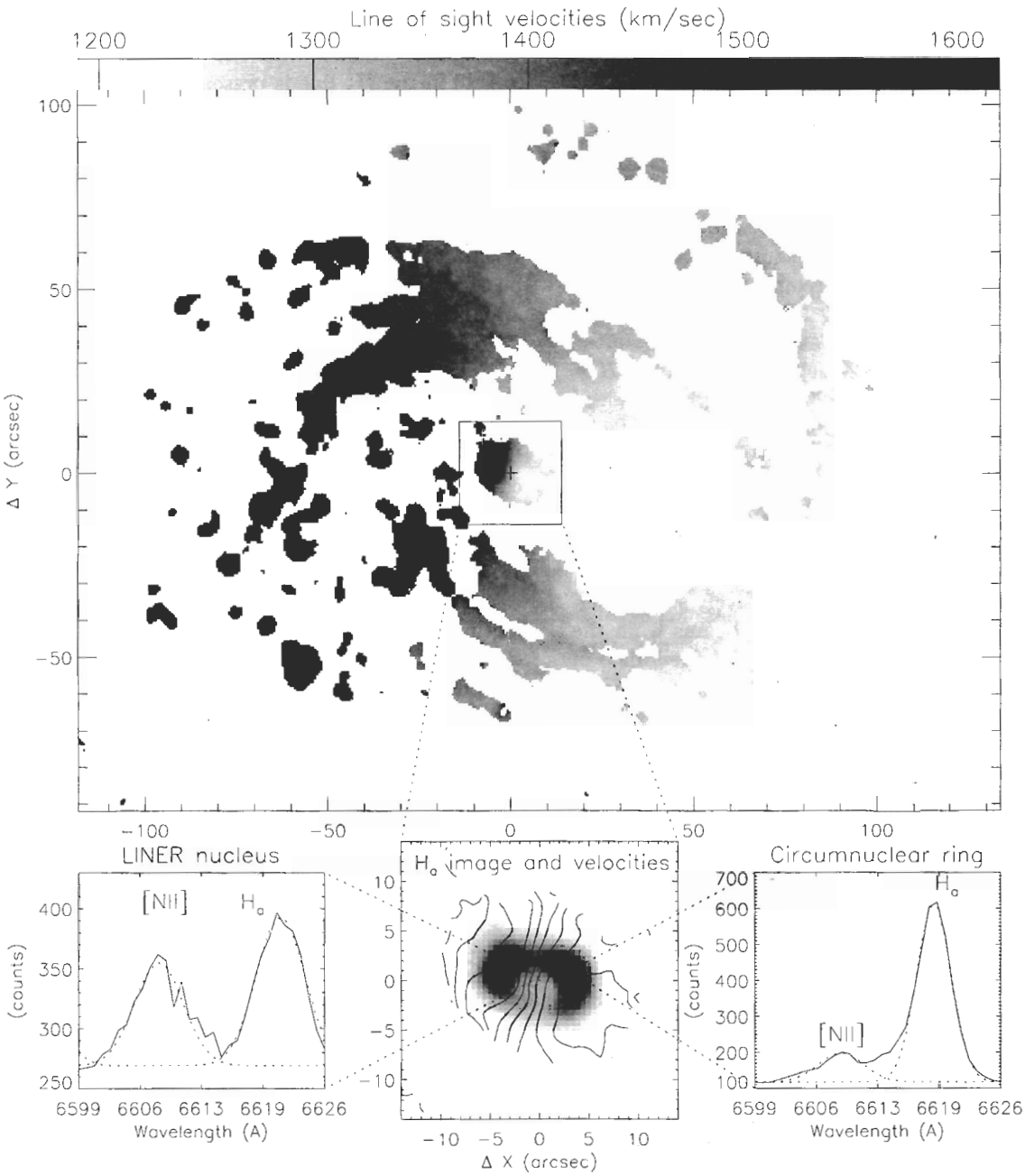

Figure 11: *Ionized gas in the galaxy NGC 6951. Top — the velocity field in the H_α line. The box cuts out the region for which the image of the circumnuclear star formation ring in H_α with lines of equal radial velocities is presented at the bottom. The right- and left-hand panels give examples of Gauss approximation of the profiles of the emission lines H_α and [NII]λ6583 in the nucleus and circumnuclear ring.*

without notable systematic difference. The velocity dispersion of stars of the cluster in the second method turned out to be somewhat lower, which is likely to suggest its higher reliability. A comparison with the published data on radial velocity of stars in this cluster shows no systematic shift in observations with the IFP. The error of individual velocity measurements of stars down to $V \sim 17\overset{m}{.}5$ estimated from a comparison of the measured velocity dispersion of stars with the literature data was $2 - 4\,\mathrm{km \cdot s^{-1}}$.

7. Conclusions

The paper presents algorithms of reduction of observations of extended objects with a scanning Fabry-Perot interferometer, which are oriented to a CCD as the detector. The distinctive feature of such observations is that the radial velocity measurement accuracy

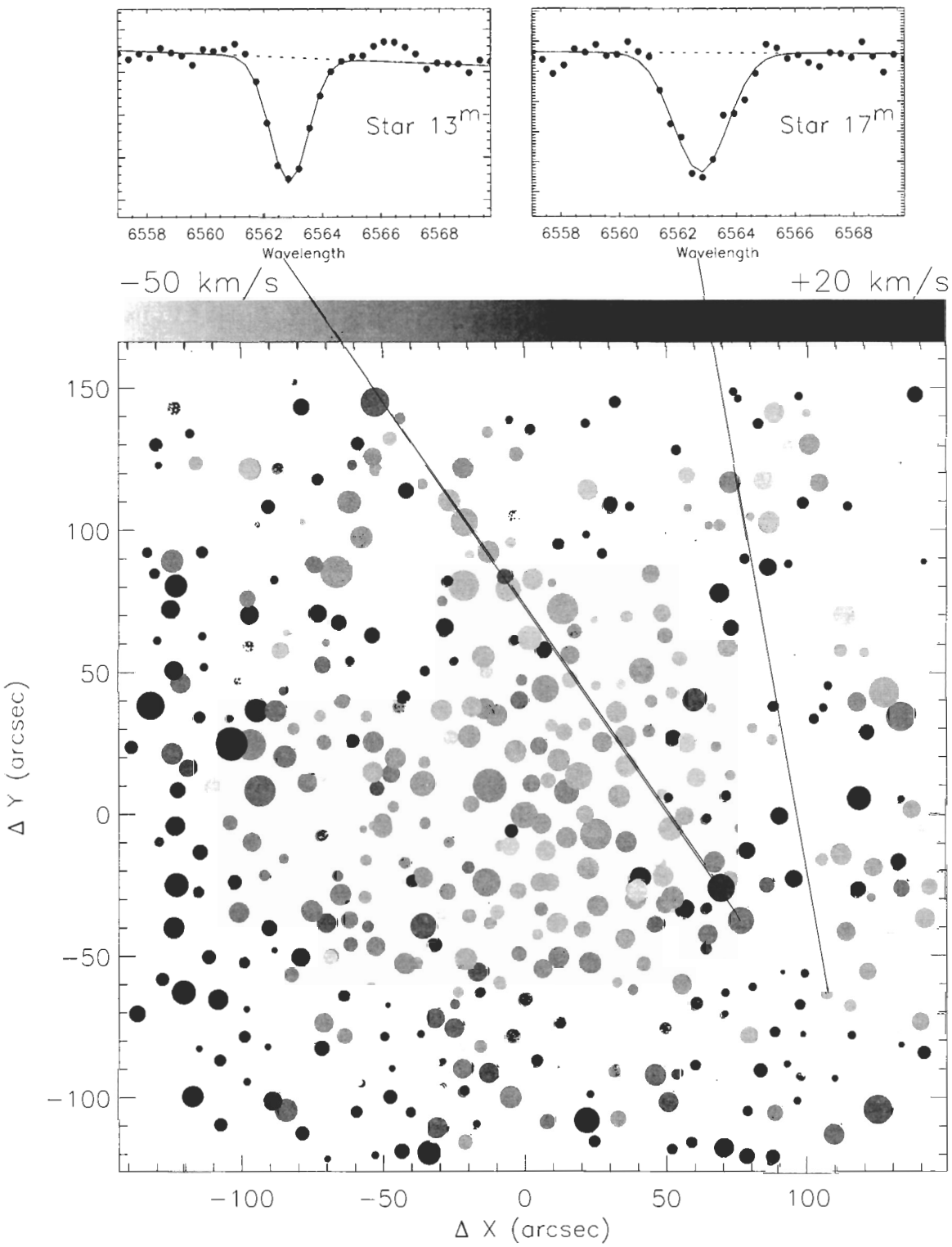

Figure 12: *Velocities of individual stars in the globular cluster M 71. The diameters of the circles are proportional to the stellar magnitude, the colour — to the radial velocity according to the scale at the top. Examples are shown of H_α absorption in the spectra of stars of $V = 13^m$ and $V = 17^m$ and their Gauss fitting.*

is often defined not by the formal value of the S/N ratio, but by the presence of spurious rings in the wavelength domain. Both the causes of their origin and the methods of their control at the stage of data reduction are studied. All the above-described algorithms are successfully applied to reduction of observations obtained with the optical reducer SCORPIO of the 6 m telescope prime focus.

Acknowledgements. The author thanks V.L. Afanasiev and T.A. Movsesian for useful comments and also N.N. Samus and A.S. Rastorguev for permission to make use of the data on M71 before their publication. The work was supported by the RFBR through grants 01-02-16118, 01-02-17597 and by the Federal Programme "Astronomy" (Project 1.2.3.1).

References

Amram P., Marcelin M., Bonnarel F., Boulesteix J., Afanas'ev V.L., Dodonov S.N., 1992, Astron. Astrophys., **263**, 69

Afanasiev et al., 2002 (in preparation)

Bland J. and Tully R.B., 1989, Astron. J., **98**, 723

Bland-Hawthorn J., 1995, ASP Conf.Ser., **71**, 72

Boulesteix J., Georgelin Y., Marcelin M., Fort J.A., 1982, in: "Instrumentation for astronomy with large optical telescopes", 223

Boulesteix J., 2000, ADHOC manual, `http://www-obs.cnrs-mrs.fr/ADHOC/adhoc.html`

Courtes G., 1960, Ann. d'Astrophys., **23**, 115

Gordon S., Koribalski B., Houghton S., Jones K., 2000, Mon. Not. R. Astron. Soc., **315**, 248

Hernandez O., Gach J.-L., Boulesteix, J., Amram P., Boissin O., Carignan C., Garrido O., Marcelin M., Oslin G., Rampazzo R., 2001, in: "Galaxies: the Third Dimension", eds.: Rosado M., Binette L., & Arias L., to be published in ASP Conf. Series

Jones D.H., Shopbell P.L., Bland-Hawthorn J., 2002, Mon. Not. R. Astron. Soc., **329**, 759

Dodonov S.N., Vlasyuk V.V., Drabek S.V., 1995, "Fabry-Perot Interferometer. Users' manual", Nizhnij Arkhyz

Osterbrock D.E., Fulbright J.P., Martel A.R., Keane M.J., Trager S.C., Basri G., 1996, Publ. Astr. Soc. Pacific, **108**, 277

Pérez, E., Márquez, I., Durret, F. González Delgaro R.M., Masegosa J., Maza J., Moles M., 2000, Astron. Astrophys., **353**, 893

Tully B.R., 1974, Astrophys. J. Suppl. Ser., **27**, 415